ORIGINAL PAPER

The impact of SST on the wind and air temperature simulations: a case study for the coastal region of the Rio de Janeiro state

Ian Cunha D`Amato Viana Dragaud[1] · Mauricio Soares da Silva[2] · Luiz Paulo de Freitas Assad[3] ·
Márcio Cataldi[4] · Luiz Landau[1] · Renato Nascimento Elias[5] · Luiz Claudio Gomes Pimentel[3]

Abstract

The impact of Sea Surface Temperature (SST) on the wind and air temperature numerical simulations over the coastal region of the state of Rio de Janeiro, Brazil, was investigated using the Weather Research and Forecasting (WRF) model. The study period comprised January 24–26, 2014, characterized by the occurrence of coastal upwelling. Two numerical experiments were performed. The first, called EGFS, used the Global Forecast System (GFS) results to prescribe the initial and boundary conditions. In the second, called EMUR, the SST was replaced by the Multi-scale Ultra-high-Resolution SST (MUR SST). The experiments showed significant differences between the SST fields, being higher than 10 °C. Through the comparison with observations, we verified that the upwelling was better represented in the EMUR, which consequently generated improvements in the temperature at 2 m above ground level (AGL) over this region. In the offshore region, over areas with higher SST, the wind speed at 10 m AGL was stronger, and opposite behavior was observed over low SST areas. In addition, in regions with higher SST differences between the experiments, differences of wind direction at 10 m AGL higher than 90° were detected. The SST influence on the air temperature and wind speed profiles was significant up to 300 and 900 m, respectively. The comparisons between the wind observations with the numerical results show that the land–sea breeze simulation (thermal forced) was underestimated in relation to the synoptic forcing (South Atlantic Subtropical Anti-cyclone), even with significant SST differences between experiments.

✉ Ian Cunha D`Amato Viana Dragaud
  iandragaud@lamma.ufrj.br

  Mauricio Soares da Silva
  soares@lamma.ufrj.br

  Luiz Paulo de Freitas Assad
  lpaulo@lamce.coppe.ufrj.br

  Márcio Cataldi
  mcataldi@id.uff.br

  Luiz Landau
  landau@lamce.coppe.ufrj.br

  Renato Nascimento Elias
  rnelias@nacad.ufrj.br

  Luiz Claudio Gomes Pimentel
  pimentel65@gmail.com

[1] Laboratory For Computer Methods in Engineering, Civil Engineering Program, Alberto Luiz Coimbra Institute of Post-Graduation and Research in Engineering (COPPE), Federal University of Rio de Janeiro (UFRJ), Avenida Athos da Silveira Ramos, 149, Cidade Universitária, Rio de Janeiro, RJ 21941-909, Brazil

[2] Mechanical Engineering Program, Alberto Luiz Coimbra Institute of Post-Graduation and Research in Engineering (COPPE), Federal University of Rio de Janeiro (UFRJ), Rio de Janeiro, RJ 21941-909, Brazil

[3] Department of Meteorology, Geoscience Institute (IGEO), Federal University of Rio de Janeiro (UFRJ), Rio de Janeiro, RJ 21941-916, Brazil

[4] Department of Agricultural and Environmental Engineering, Post Graduation in Biosystems Engineering, Fluminense Federal University (UFF), Niterói, RJ 24210-240, Brazil

[5] Civil Engineering Program, High Performance Computing Center, Alberto Luiz Coimbra Institute of Post-Graduation and Research in Engineering (COPPE), Federal University of Rio de Janeiro (UFRJ), Rio de Janeiro, RJ 21941-909, Brazil

1 Introduction

Coastal regions are one of the greatest natural and economic resources on the planet. These regions are characterized by high population densities, where are developed activities related to ports, airports, oil companies, tourism and others, which most of the time need accurate numerical weather predictions (NWP) to give support to their operations. Three different environments compose coastal regions: ocean, atmosphere and land surfaces. These environments exchange matter and energy through their boundaries.

On land surfaces, higher temperature variations occur daily due to the low molecular conductivity and low heat capacity. In contrast, the high heat capacity of sea water causes diurnal low Sea Surface Temperature (SST) variations. These different heat capacities of the land and the sea water generate a mesoscale land–sea horizontal temperature gradient that results in a horizontal pressure gradient which drives the land–sea breeze circulation. This phenomenon is able to form when synoptic scale forcing is not sufficiently strong to overcome the land–sea gradients (Stull 1988). Beyond the land–sea breeze, areas over the land with different land use could generate temperature gradient that also drives thermally induced circulations and the same process occurs over the ocean with surface water masses characterized by different temperatures.

NWP models are important tools capable of representing the diurnal variations of the wind field related with land–sea breezes (e.g., Knievel et al. 2010; Jeong et al. 2012; Phan and Manomaiphiboon 2012; Tseng et al. 2012; Moisseeva and Steyn 2014; Jiménez et al. 2016) and variations induced by SST gradients (e.g., Song et al. 2006; O'neill et al. 2010; Shimada et al. 2015).

Some studies deal with the sensitivity of the low-level atmospheric flow in relation to improvements on the SST field representation that is used as initial and boundary conditions in NWP models. Despite the use of high-resolution SST fields does not necessarily produce improvements on land–sea breeze representation (LaCasse et al. 2008; Knievel et al. 2010), it could have vital importance for accurate simulation of the ocean–atmosphere interaction processes (Song et al. 2009).

SST is one of the primary indicators of climate variability (e.g., Santos et al. 2013; Chen et al. 2018). In climate models, a better representation of SST improves the ocean–atmosphere interaction processes, the teleconnections involving these interactions and the different monsoon regimes occurring around the globe (e.g., Cataldi et al. 2010; Kucharski et al. 2010; da Silva et al. 2018). In both studies of seasonal climate forecast and climate change, the variability of the ocean determines the atmospheric behavior. Therefore, a better representation of the ocean as initial and boundary conditions consequently generates a better modeling of the atmosphere also on these scales. The fact is that the SST is a critical parameter for climate modeling. Despite this, it also can be a key parameter to improve the NWP of some regions in the world. The NWP model performance will depend on the regional geophysical characteristics, which present processes of different complexities.

Nowadays, many gap-free SST products are available for the scientific community, each with its own characteristics. These products are generated by methodologies that combine satellites measurements and in situ data (Martin et al. 2012; Dash et al. 2012). Messager and Faure (2012) and Shimada et al. (2015) observed that SST fields from the Global Forecast System (GFS) do not represent oceanic mesoscale features. Dufois et al. (2012) found that SST products overestimate nearshore values where high SST gradients exist, presenting systematic errors. In these regions, the SST fields are not representative during peak upwelling season (Dufois et al. 2012).

Over the Brazilian Southeast continental shelf, in the vicinity of state of Rio de Janeiro, strong SST gradients occur associated with the coastal upwelling (Castro and Miranda 1998; Rodrigues and Lorenzetti 2001; Franchito et al. 2008; Castelão 2012; Mazzini and Barth 2013; Palóczy et al. 2014). The localization and magnitude of these gradients are variable among SST products (Castelão 2012), impacting the NWPs.

Limited-area numerical models were applied to the state of Rio de Janeiro in order to simulate the local atmospheric circulation. Paiva et al. (2014) and Giannaros et al. (2017) verified, as a general pattern, satisfactory performance of the simulations for the metropolitan area of Rio de Janeiro. Otherwise, there are errors in the sea breeze representation at this region (Paiva et al. 2014; Pimentel et al. 2014a). Franchito et al. (1998) and Ribeiro et al. (2011, 2016) indicated a strong sensitivity of the numerical simulation of wind field due to SST variations in the upwelling region.

To obtain a better numerical representation of the coastal region of the state of Rio de Janeiro, this study investigates the use of two SST products for the initial and boundary conditions to the Weather Research and Forecasting (WRF) model and its impacts on air temperature and near-surface atmospheric flow.

2 Study region

The coastal region of the state of Rio de Janeiro has been highlighted in several studies due to its high degree of physiographic, oceanographic and meteorological complexity, which makes this region extremely challenging from the

NWP point of view (Oliveira Júnior et al. 2010; Ribeiro et al. 2011; Pimentel et al. 2014a, b; Paiva et al. 2014; Brito et al. 2016; Aragão et al. 2017; Silva et al. 2017).

The state is located in Southeastern part of Brazil. It has borders with the Atlantic Ocean and the states of São Paulo (SP), Minas Gerais (MG) and Espírito Santo (ES) (Fig. 1). The coastline has approximately 635 km of extension (Brito et al. 2016), with capes and bays. The East and Central Coasts are characterized by an extensive lowland area, while on the West Coast there is great topographic variation (Fig. 1). The soil use and occupation are nonhomogeneous, with the predominance of forest, urban and restinga areas (Scheel-Ybert 2000; Paiva et al. 2014).

On the synoptic scale, the South Atlantic Subtropical Anticyclone (SASA) is the dominant feature that predominantly influences the state of Rio de Janeiro (Dereczynski and Menezes 2015). This system drives the prevailing surface winds to blow from the first quadrant (0°–90°) along the East Coast, combined with the land–sea breeze circulation (Franchito et al. 2008; Dereczynski and Menezes 2015). Specifically, in the Arraial do Cabo region (Fig. 1), the winds become more zonal and intense during the afternoon because of the sea breeze intensification (Franchito et al. 2008). In the Central and West Coasts, the land–sea breeze circulation overcomes the SASA winds, driving the near-surface flow and producing a wind regime perpendicular to the coastline (Pimentel et al. 2014b; Paiva et al. 2014).

In the East and Central Coasts, the SASA prevailing winds together with the orientation of the coastline are highly upwelling favorable, characterized by low SST near the coast (Emilson 1961; Ikeda et al. 1974; Valentin et al. 1987; Castelão and Barth 2006; Franchito et al. 2008; Palóczy et al. 2014) that influence the local circulation (Franchito et al. 1998; Ribeiro et al. 2011). During the passage of frontal systems, the winds blow from the southern quadrant inhibiting the upwelling (Valentin et al. 1987; Stech and Lorenzzetti 1992; Dourado and Oliveira 2000).

3 Data and methods

3.1 Period

The study period comprised January 24–26, 2014, characterized by the continuous occurrence of coastal upwelling in the Central and East Coast and dominance of the SASA over the state. Under this condition, the SST gradients varied significantly between the SST products, which favor the WRF model sensitivity evaluation. Since the upwelling in this region is characterized by SST values below 18 °C (Calado
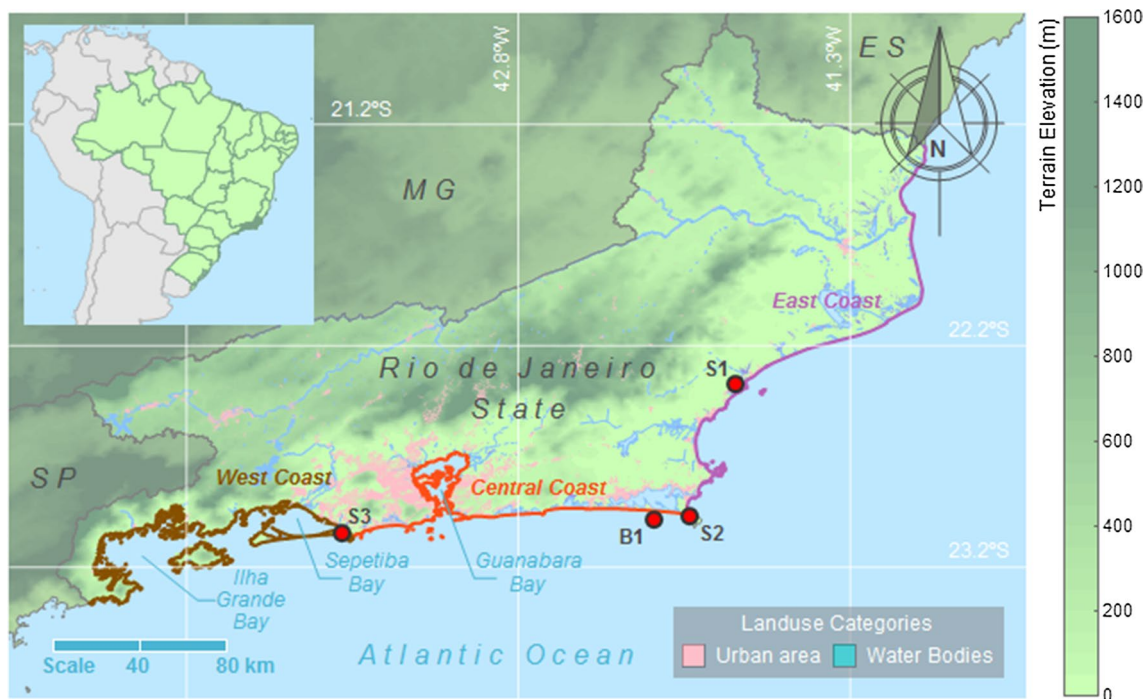
Fig. 1 State area and location in Brazil. S1, S2 and S3 indicate the surface weather observation stations sites of Macaé, Arraial do Cabo and Marambaia, respectively, and B1 indicates the buoy site. The elevation and the land use categories of the urban area and water bodies are also shown. SP, MG and ES are the state abbreviations of São Paulo, Minas Gerais and Espírito Santo, respectively. The coastline was divided into West, Central and East Coasts to facilitate the following analyses

et al. 2010; Cerda and Castro 2014), the study period was defined through the buoy SST observations (Fig. 1).

3.2 WRF model and experiments

The simulations are performed with the WRF model (Skamarock et al. 2008) version 3.6. The model is configured with a total of three domains applying a telescopic one-way nesting. The hierarchy of the WRF grids is illustrated in Fig. 2. The horizontal resolutions of the coarse (d01), intermediary (d02) and finest (d03) domains are 27, 9 and 3 km, respectively. All the three nested domains were configured with the same stretched vertical grid with 35 levels, including seven levels below 1 km.

It is important to emphasize that in the WRF model, horizontal velocity components and thermodynamic prognostic variables are assigned to the half-σ levels (Skamarock et al. 2008; Shin et al. 2012). Moreover, the WRF results on the lowest half-σ level are used in the surface layer parameterization to diagnose the wind at 10 m AGL and the T2m, at their typical observational heights (Jimenez et al. 2012; Shin et al. 2012; Ma et al. 2014). In the present simulations, the first half-σ level is located around 29 m above ground level (AGL). In the surface layer

parameterization used in this study, the Revised MM5 Monin-Obuckov (Jimenez et al. 2012), the T2m and the wind at 10 m AGL are diagnosed according to the Eqs. (1) and (2), respectively:

$$\theta_{2m} = \theta_g + (\theta_a - \theta_g)\frac{\ln\left(\frac{2+z_0}{z_0}\right) - \Psi_h\left(\frac{2+z_0}{L}\right) + \Psi_h\left(\frac{z_0}{L}\right)}{\ln\left(\frac{z+z_0}{z_0}\right) - \Psi_h\left(\frac{z+z_0}{L}\right) + \Psi_h\left(\frac{z_0}{L}\right)} \quad (1)$$

$$u_{10m} = u_a\frac{\ln\left(\frac{10+z_0}{z_0}\right) - \Psi_m\left(\frac{10+z_0}{L}\right) + \Psi_m\left(\frac{z_0}{L}\right)}{\ln\left(\frac{z+z_0}{z_0}\right) - \Psi_m\left(\frac{z+z_0}{L}\right) + \Psi_m\left(\frac{z_0}{L}\right)} \quad (2)$$

where u_{10m} is the wind at 10 m AGL, θ_{2m} is the temperature at 2 m AGL, θ_g is the ground surface potential temperature, L is the Obukhov length, z_0 is the roughness length, $\Psi_{m,h}$ are the integrated similarity functions for momentum and heat. z is the lowest half-σ level height, and u_a and θ_a are the wind and air temperature in this level.

The Moderate Resolution Imaging Spectroradiometer (MODIS) data set is employed to represent the land use and the United States Geological Survey (USGS) data set

Fig. 2 The three nested model domains used in WRF. The elevation is also shown
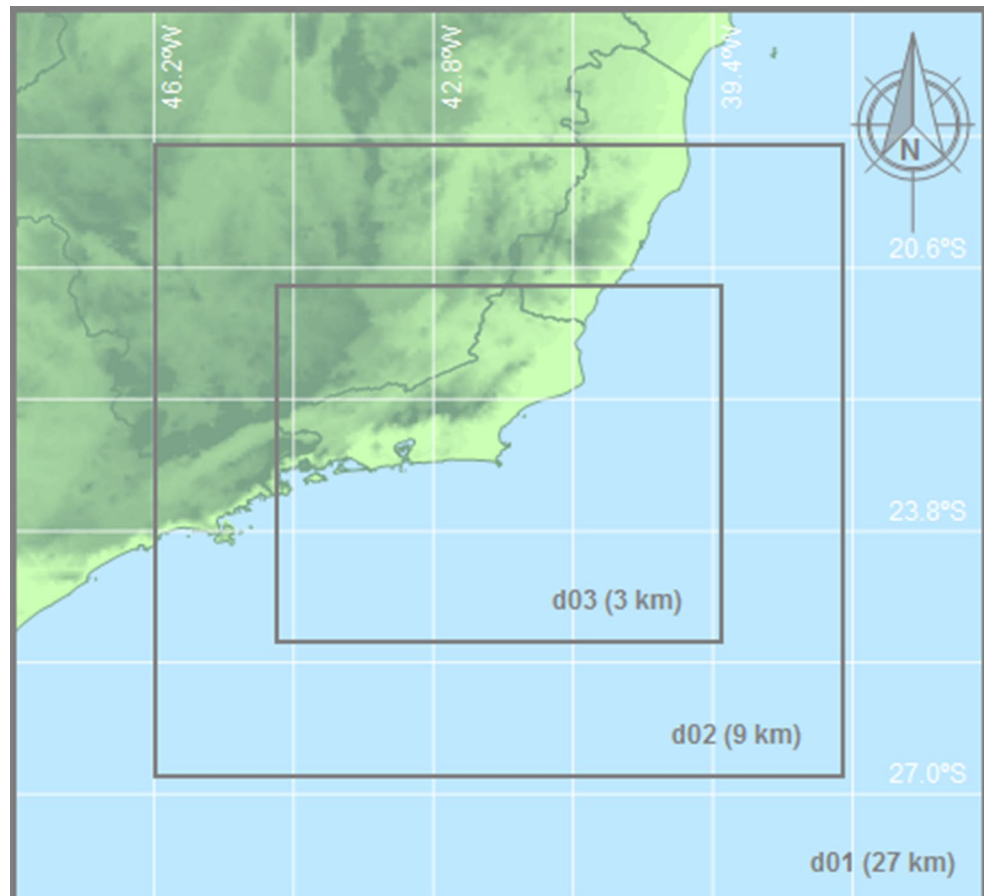
is employed to represent the topography height, both at 1 km resolution.

Physical parameterizations include the rapid radiative transfer model longwave radiation (Mlawer et al. 1997), the Dudhia shortwave radiation scheme (Dudhia 1989), the WRF single-moment three-class microphysics scheme (Hong et al. 2004), the Betts–Miller–Janjic cumulus parameterization scheme (Janjic 1994), the Noah-MP land surface model (Niu et al. 2011; Yang et al. 2011), the Revised MM5 Monin-Obuckov (Jiménez et al. 2012) for surface layer, and the Grenier–Bretherton–McCaa Planetary Boundary Layer scheme (Grenier and Bretherton 2001).

Initial and lateral boundary conditions from GFS forecast results (http://www.emc.ncep.noaa.gov/GFS/doc.php) were provided to the WRF model. The GFS forecast results have 3-h intervals, a horizontal resolution of 0.5° × 0.5° and came from the simulation initialized at 00 UTC 24 January 2014.

Two sets of numerical simulations were performed using the WRF model. The first experiment, hereafter called EGFS, used the GFS forecast results to prescribe the initial and boundary conditions. The second, from now called EMUR, was identical to the EGFS, except that the SST from GFS was replaced by the Multi-scale Ultra-high-Resolution Sea Surface Temperature (MUR SST). Although at each GFS forecast result there is a new SST field, to match the temporal resolution of the SST between the numerical experiments, the SST boundary condition was updated daily in both experiments because the MUR SST analysis is a daily product.

3.3 SST products

The GFS SST initial and boundary conditions are composed by the weekly 1° (~ 111 km) spatial resolution optimum interpolation SST analysis (Reynolds et al. 2002). This product is based on a blending of in situ observations from ships and buoys and satellite observations from the infrared Advanced Very High-Resolution Radiometer (AVHRR). The GFS SST temporal variation is described by Eq. (3):

$$SST(t) = SSTc(t) + SSTa(t = 0) \times e^{\left(-\frac{t}{\tau}\right)} \qquad (3)$$

where t is the time, $SST(t)$ is the SST at time t, $SSTc(t)$ is the climatological SST at time t, $SSTa(t = 0)$ is the initial SST anomaly, and τ is the decaying time scale of initial SST anomaly, with a value of 90 days (Fu et al. 2013). The initial SST anomaly is given by Eq. (4):

$$SSTa(t = 0) = SST(t = 0) - SSTc(t = 0) \qquad (4)$$

The MUR SST analysis is a daily product, globally gridded at approximately 1 km resolution by merging data from the AVHRR, the MODIS, and the Advanced Microwave Scanning Radiometer for the Earth Observing System

(AMSR-E). More information can be found at http://mur.jpl.nasa.gov/ and data descriptions may also be found at http://podaac.jpl.nasa.gov/dataset/JPL-L4UHfnd-GLOB-MUR. This product was used to study upwelling and thermal fronts regions in the Gulf of Guinea (Wiafe and Nyadjro 2015), the Coasts of Peru (Vazquez-Cuervo et al. 2013), Chile (Bravo et al. 2016) and Brazil in the vicinity of state of Rio de Janeiro (Macedo and Lorenzzetti 2015; Mill et al. 2015; Fragoso et al. 2016).

3.4 Observed data

Three surface weather observation stations were selected from the INMET (National Meteorology Institute of Brazil) located in the coastal region, in the cities of Macaé (S1 in Fig. 1), Arraial do Cabo (S2 in Fig. 1) and Rio de Janeiro (S3 in Fig. 1). We use hourly observational data of wind speed and direction at 10 m AGL, and temperature at 2 m AGL (T2m).

The buoy was moored in the vicinity of Arraial do Cabo city (B1 in Fig. 1) by Sistema Integrado de Obtenção de Dados Oceanográficos project (SIODOC), at approximately 5 km from the coast. We use hourly observational data of wind speed and direction, air temperature and SST. The atmospheric variables are measured at 3.5 m above sea level. The SST is measured at 0.5 m depth, referred to as bulk temperatures (Lazarus et al. 2007). We applied the neutral logarithmic wind profile law (Eq. 5) to adjust the buoy wind speed data, and so standardize the weather measurements (World Meteorological Organization 2008).

$$u_{10} = u_{3.5} \frac{\ln\left(\frac{10}{z_0}\right)}{\ln\left(\frac{3.5}{z_0}\right)}. \qquad (5)$$

where z_0 is the aerodynamic roughness length, u_{10} and $u_{3.5}$ are to the wind speeds at 10 and 3.5 m, respectively. To estimate z_0, the Charnock relation (Charnock 1955) is applied.

3.5 Analyses

Results from both experiments using the high-resolution grid (3 km) will be presented. The first 6 h are discarded as a spin-up. We analyze the fields of each numerical experiment and difference fields between the experiments ([EMUR − EGFS]) for 25 January 2014. The SST field is analyzed daily, while the T2m and the wind at 10 m AGL fields are analyzed at 06 and 18 UTC. The wind direction differences between the experiments were calculated following Jiménez and Dudhia (2013). The differences represent the smaller angle between the vectors and the values are in the range [− 180°, 180°]. This definition assigns positive (negative)

differences if the EMUR is rotated clockwise (counterclockwise) with respect to the EGFS wind vector.

In addition, the vertical–longitudinal cross sections of differences in air temperature and wind intensity between the experiments ([EMUR − EGFS]) were analyzed. The sections were averaged over the entire study period along 23.3°S.

The model results were compared with the observational data through time series of SST, T2m and wind at 10 m AGL. The model results from the lowest level were not compared directly with the observational data, since they are not at the same height. To conduct a rigorous analysis, the observed wind at 10 m AGL and temperature at 2 m AGL were compared with the wind and the air temperature diagnosed in the surface layer parameterization at the same height (Eqs. 1, 2). Besides that, it was realized a careful selection of the grid points. In this way, the results from the grid points on land that are nearest to the surface weather observation stations sites are compared with the observations taken over this sites. Similarly, the results from the grid point on the water that is nearest to the buoy site are compared with the buoy data. It must be noted that no interpolation was applied.

4 Results and discussion

4.1 SST fields

The bigger differences between the EGFS SST and the EMUR SST occur close to the coast (Fig. 3c), which highlights the importance of assessing the SST products for coastal regions. While in the East and Central Coasts there are intense gradient and lower SST values in the EMUR (22 °C) related to the upwelling (Fig. 3b), in the EGFS there are a weak gradient and higher SST values (26 °C) (Fig. 3a). These differences are more prominent in Fig. 3c. On the West Coast, the pattern is inverse, strong gradient and the lowest SST values are in the EGFS, with differences of up to

10 °C between the experiments (Fig. 3c). The spatial pattern found in the EMUR SST field is in agreement with earlier studies (Castro and Miranda 1998; Rodrigues and Lorenzetti 2001; Franchito et al. 2008; Castelão 2012; Palóczy et al. 2014).

4.2 Meteorological fields

4.2.1 Temperature at 2 m AGL

Over the ocean, the T2m (Fig. 4) primarily responded to SST, following the same spatial pattern of the SST fields (Fig. 3). Over the land surface, the difference of T2m between the two experiments was not as intense as over the ocean. This result was already expected since only the ocean boundary condition was modified (i.e., the SST) and it agrees with numerical results from Ribeiro et al. (2011). Tseng et al. (2012) found that SST greatly influences the T2m AGL over the ocean and over the continent.

The thermal amplitude over land was greater because of the smaller soil specific heat compared to the ocean, producing a land–sea thermal gradient (Fig. 4). In the EMUR, it was represented a greater (lower) thermal gradient on the West Coast and a lower (greater) gradient on the Central and East Coasts, in comparison with the EGFS at 06 UTC (18 UTC). Thus, the gradients varied in space and time, modifying the thermal forcing between the experiments.

4.2.2 Wind at 10 m AGL

The wind fields showed that the different regions of the coast of the state of Rio de Janeiro were driven by the same forcing mechanisms in both numerical experiments (Fig. 5). The wind at 10 m AGL near the coast resulted from the combined contribution of the synoptic forcing, the SASA, and the thermally induced mesoscale forcing, the land–sea breeze. The synoptic contribution induced the flow to blows from the first quadrant (0°–90°), while the breeze depended on the coastline and the period of the day.
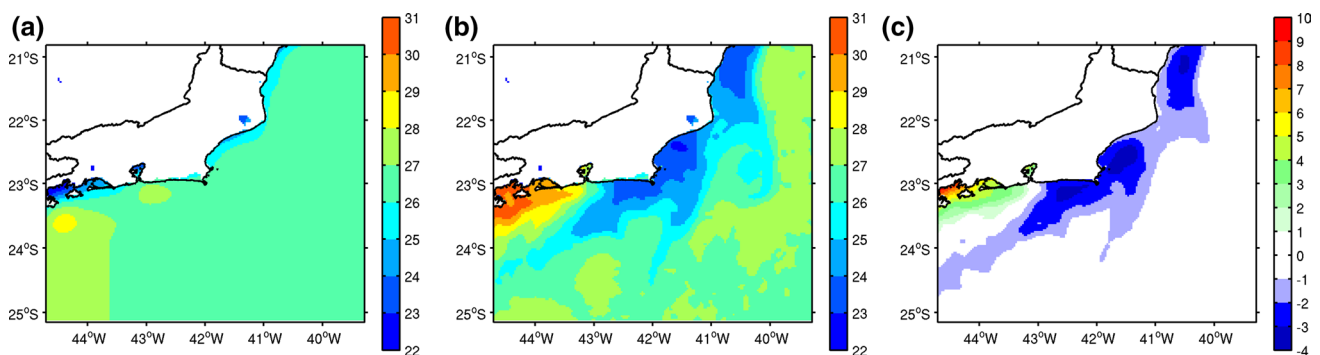
Fig. 3 SST fields (°C) on 25 January 2014: **a** EGFS, **b** EMUR, **c** difference between the experiments [EMUR − EGFS]

Fig. 4 Temperature at 2 m AGL fields (°C) on 25 January 2014 at 06 UTC (left) and at 18 UTC (right): **a**, **b** EGFS, **c**, **d** EMUR, **e**, **f** difference between the experiments [EMUR − EGFS]
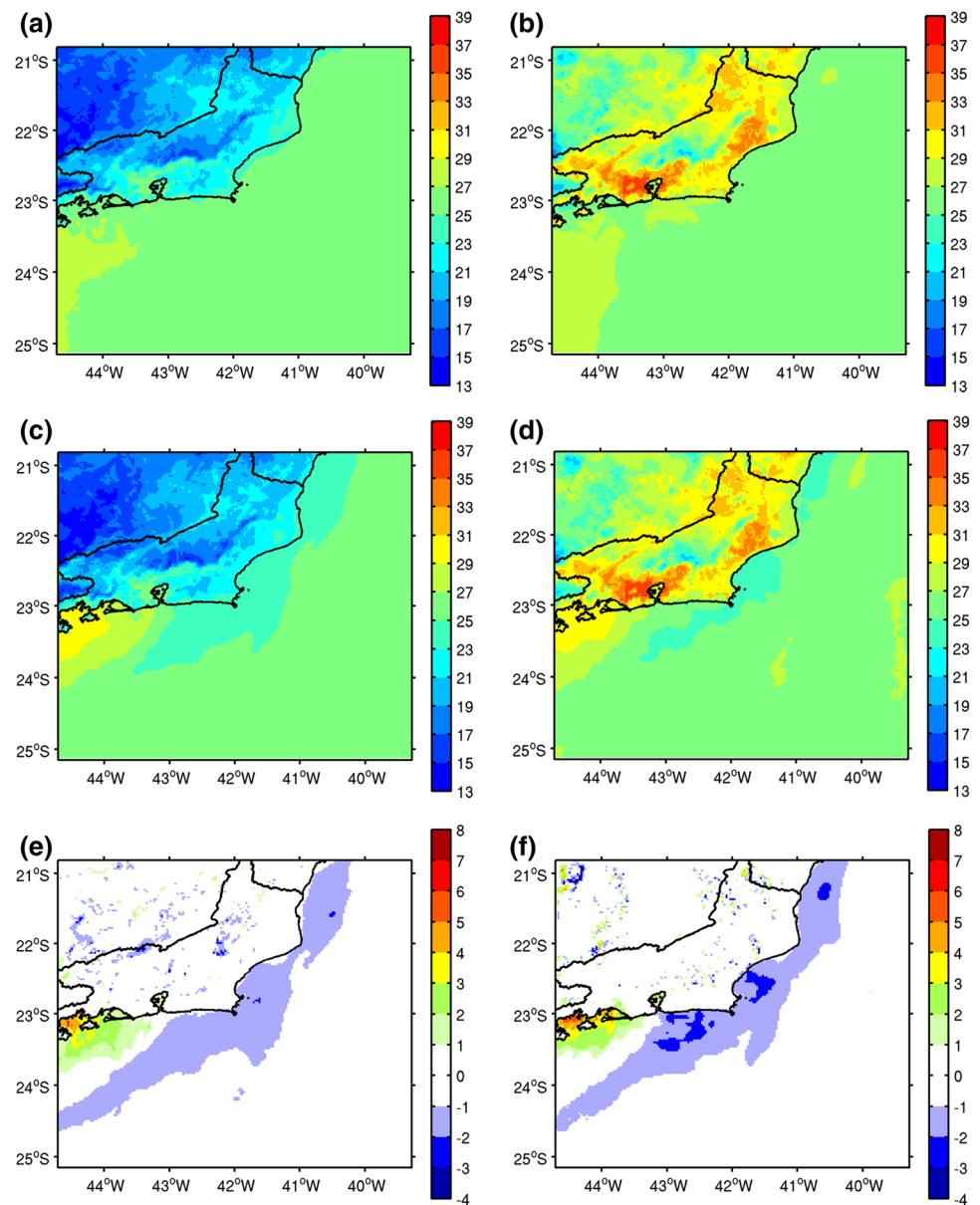

On the East Coast, the predominance of north to northeast winds at 06 UTC indicates the dominant influence of SASA in relation to the land breeze, since the latter should induce west winds. At 18 UTC, the wind direction tended towards the east on the East Coast, evidencing the sea breeze occurrence at this period. On the Central and West Coasts, despite the SASA influence, the land–sea breeze was more evident than on the East Coast. At 06 UTC, the winds blow from the northern quadrants (270°–90°) in both simulations, characteristics of the land breeze (Fig. 5a, c). At 18 UTC, the occurrence of prevailing east and southeast winds over the coastal region shows that the near-surface flow is mainly driven by sea breeze (Fig. 5a–d). These patterns were observed in Franchito et al. (2008) and Pimentel et al. (2014b). However, as the flow approaches the mountains,

it could be also synergistically influenced by the anabatic wind.

Despite the agreement on the forcing mechanisms between the experiments (Fig. 5a–d), the disparities in the thermal forcing intensity in each numerical experiment induced modifications in the near-surface flow (Fig. 5e–h). Regardless of the analyzed period (i.e., 06 UTC or 18 UTC), it was verified in both experiments the same pattern in the wind at 10 m difference (Fig. 5e, f). In the East Coast and the eastern portion of the Central Coast, where the EMUR showed the lowest SST values related to the upwelling, the wind was weaker in the EMUR as compared to that in the EGFS. In the West Coast and the western portion of the Central Coast, where the EMUR SST was higher, the wind was stronger compared to the EGFS. These modifications of

Fig. 5 Wind at 10 m fields on 25 January 2014 at 06 UTC (left) and at 18 UTC (right). Wind speed (ms⁻¹) (shaded background) and wind vector (overlay): **a**, **b** EGFS, **c**, **d** EMUR. Difference between the experiments [EMUR − EGFS] for **e**, **f** wind speed and **g**, **h** wind direction. The wind vectors from EMUR (green) and EGFS (black) are overlaid to the wind direction differences in **g**, **h**
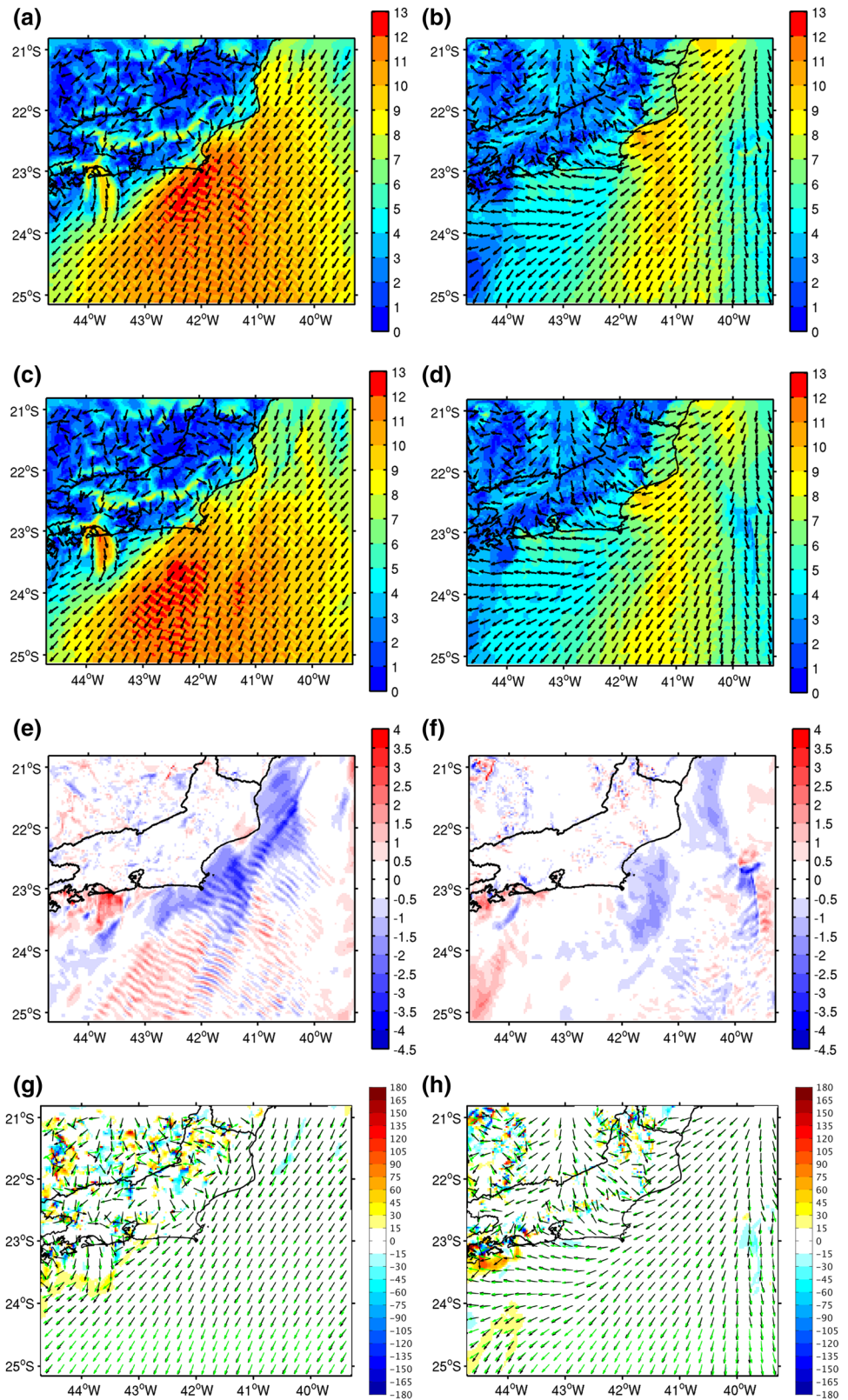
the near-surface winds by SST gradients are in accordance with the pattern described in several studies (e.g., Sweet et al. 1981; Jury and Walker 1988; Wallace et al. 1989;

Hayes et al. 1989; Wai and Stage 1989; Hashizume et al. 2002; O'neill et al. 2010; Shimada et al. 2015; Sproson and Sahlée 2014; Seroka et al. 2015). Over higher SST, the

vertical mixing results in a transfer of momentum from the upper boundary layer towards the surface, increasing the near-surface winds. However, over lower SST the process is inverse, producing weaker near-surface winds.

If on the one hand, the model responded coherently and systematically to this physical process in the offshore region, on the other hand, on a smaller spatial scale, the model was not sensitive to the land–sea gradient variation near the coastline in large part of the coast. Since at 18 UTC the T2m increase over the continent occurred in both experiments, the lower EMUR SST in the East Coast led to a greater land–sea thermal gradient, which should increase the wind intensity, in comparison to the EGFS. Likewise, the EMUR should represent weaker winds than the EGFS in the West Coast, due to the higher SST which resulted in a lower land–sea thermal gradient at 18 UTC. This low sensitivity of the WRF model in the land–sea breeze representations in relation to SST modifications was reported by LaCasse et al. (2008).

The wind direction fields did not present significant differences between the experiments in most of the domain, the Central and East Coasts (Fig. 5g, h). This result shows that even with SST differences of up to 4 °C between the experiments, the model still represented the dominance of the synoptic forcing (SASA) in relation to the mesoscale forcing (land–sea breeze) driving the near-surface flow. Exclusively on the West Coast, the numerical experiments showed significant wind direction differences, higher than 90°, where SST differences of up to 10 °C are verified. The explanation for this wind direction difference between the experiments is the flow divergence near 23.25°S and 44.25°W, present only in the EGFS. This divergence occurs due to the lower SST in this region, inducing at the same time the sea breeze and an offshore flow directed to higher SST values. A similar result was obtained by Ribeiro et al. (2011) for the region of Arraial do Cabo.

4.3 Cross sections

To determine the mean vertical reach of the SST impact on the atmosphere of the coastal region, vertical–longitudinal cross sections of differences in air temperature (Fig. 6a) and wind intensity (Fig. 6b) between the experiments were defined at a latitude of 23.3°S, which highlights the West and Central Coasts.

There were two regions well delimited by the SST impact: the West Coast, marked by higher air temperatures, and the Central Coast, predominated by lower air temperatures in the EMUR in comparison to the EGFS (Fig. 6a). The SST influence on the air temperature profile decreased with height, noted up to around 300 m above sea level, where the maximum differences are ± 0.5 °C. Near the surface, between 0 and 100 m AGL, the different SST products induced more intense effects, with differences between the experiments that ranged from $+3$ to -2 °C depending on the longitude. This result is consistent with that reported by Sproson and Sahlée (2014).

For the wind profile, the SST impact was noted up to about 950 m above sea level, where variations of up to ± 0.5 ms^{-1} are verified (Fig. 6b). The comparison between the experiments showed the predominance of stronger winds in the EMUR in the West Coast (Fig. 6b). In the Central Coast between 0 and 100 m above sea level, the strongest winds were verified in the EGFS, while in higher altitudes this was observed in the EMUR. This result reinforces the discussion presented in Sect. 4.2.2, where it was shown a positive correlation between the wind intensity at 10 m AGL and underlying SST variations. However, the vertical cross-section result indicates that this positive correlation is restricted up to 100 m above sea level (Fig. 6b). These results agree with that observed by Sproson and Sahlée (2014) and Seroka et al. (2015).

Fig. 6 Vertical–longitudinal cross sections of differences in **a** air temperature (°C) and **b** wind intensity (ms^{-1}) between the experiments [EMUR − EGFS] up to 1.0 km at 23.3°S. The dashed black lines in **a** and **b** delimits the Central and West Coasts
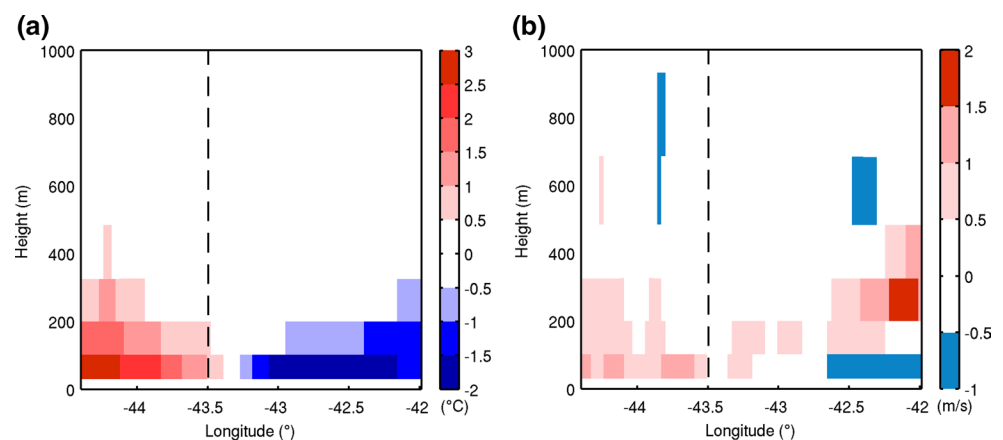
4.4 Observations and model verification

4.4.1 SST

The observed SST at the buoy in the Central Coast was lit-tle influenced by the diurnal cycle of solar radiation and, besides, there were significant differences between the numerical results against the buoy observations (Fig. 7). The observed SST is overestimated by up to 7.6 and 10.6 °C, respectively, to the EMUR and the EGFS (Fig. 7). However, the superiority of the EMUR SST stands out, since the val-ues are 3 °C lower than EGFS SST. Although the satellite-derived SST products have been evolving, this result shows the difficulty of satisfactorily representing the upwelling, corroborating studies for several regions in the world (e.g., Dufois et al. 2012; Messager and Faure 2012; Tseng et al. 2012; Peres et al. 2017). Specifically for the study region, Peres et al. (2017) found a positive bias, between satellite-derived SST products and buoy data that can reach 5 K dur-ing simultaneous upwelling events and atmospheric sub-sidence over coastal waters. The authors explain that the unexpected errors are due to water vapor compression in the lower atmospheric layer related to a temperature inversion and low SST values.

4.4.2 Temperature at 2 m AGL

Over the sea, at the buoy site (Fig. 1), the simulations over-estimate the observed T2m AGL (Fig. 8a), similar to the pattern observed for the SST (Fig. 7). However, the better representation of the SST in EMUR improves the T2m simu-lation by WRF in up to 2 °C (Fig. 8a).
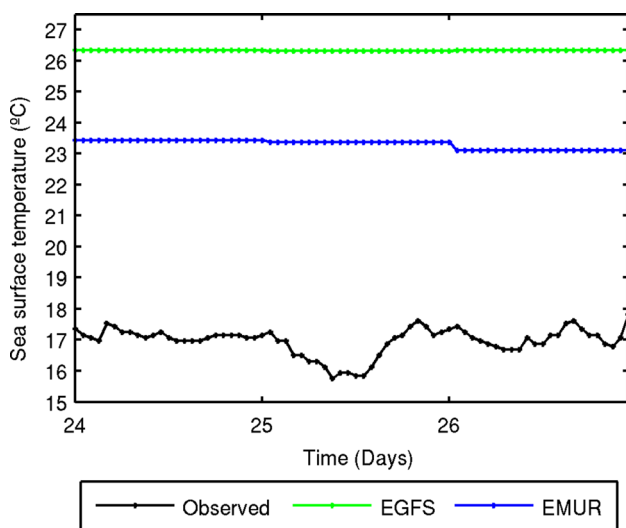
Fig. 7 Time series of the observed and simulated SST (°C) at the buoy site

Following the same pattern of the SST (Fig. 7), the observed T2m at the buoy also does not presented a temporal variation exclusively directed by the diurnal cycle of solar radiation (Fig. 8a). However, the numerical results show a well-defined diurnal cycle of T2m for the 3 days, disagreeing with the observed pattern. Theoretically, the air temperature variation inside the surface layer is mainly driven by the longwave radiation from the surface, following the intensity variation over time (Ahrens 2009). Intriguingly, the numeri-cal experiments which do not represent diurnal SST varia-tion, produce a diurnal cycle of T2m, suggesting that another process not so apparent in the observed data is influencing the model results. This process can be the horizontal advec-tion of heat. Besides this, it can be noted some fluctuations of the T2m observed at the buoy site. These fluctuations are possibly related to changes in the position of the temperature sensor generated by waves, and related to transport of heat by eddies, which are not well represented by the model.

Over the land surface, the different representations of the SST also impacted the T2m. In these cases, Arraial do Cabo (Fig. 1) was the most sensitive site in relation to the different SST products used (Fig. 8b), the site with the great-est influence of the upwelling. At this spot, the simulations also overestimate the observed T2m, similar to the results obtained for the buoy site. Despite these systematic errors, there are also consistent improvements in the T2m repre-sentation in the EMUR, especially during the night. The largest errors in the T2m representation at Arraial do Cabo site happen during the daytime period (Fig. 8b) when the sea breeze occurs. Since the model represents higher tem-peratures than observed over the sea (Fig. 8a), the advection of this maritime air by the breeze contributes to the T2m overestimation over the land surface. The T2m AGL was also improved with better SST representation in other studies (e.g., LaCasse et al. 2008; Knievel et al. 2010).

At the sites of Macaé in the East Coast and Marambaia in the border between the Central and West Coasts (Fig. 1), no significant differences between the simulated T2m by the numerical experiments are evident (Fig. 8c, d). Both experiments represent the observed diurnal cycle of T2m in both sites. The maximum simulated values were close to those observed, with temporal lags, more evident at Mar-ambaia site. In relation to the T2m minimums, the WRF results underestimate the observations with differences of up to 4 °C on 25 January 2014.

4.5 Wind at 10 m AGL

As previously indicated, the analysis of the wind at 10 m AGL at the evaluated sites (Fig. 9) confirms the combined contribution of two meteorological systems: the SASA, the synoptic scale system, and the land–sea breeze circulation,
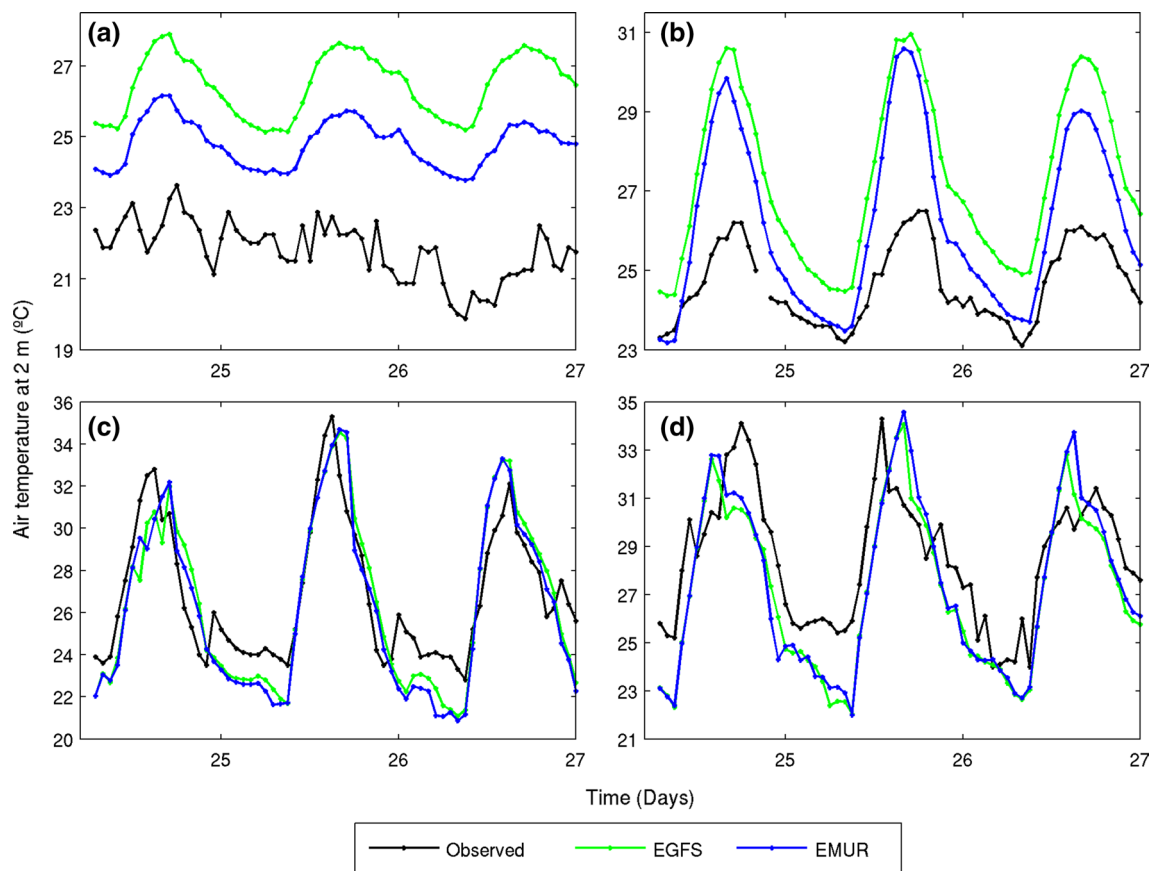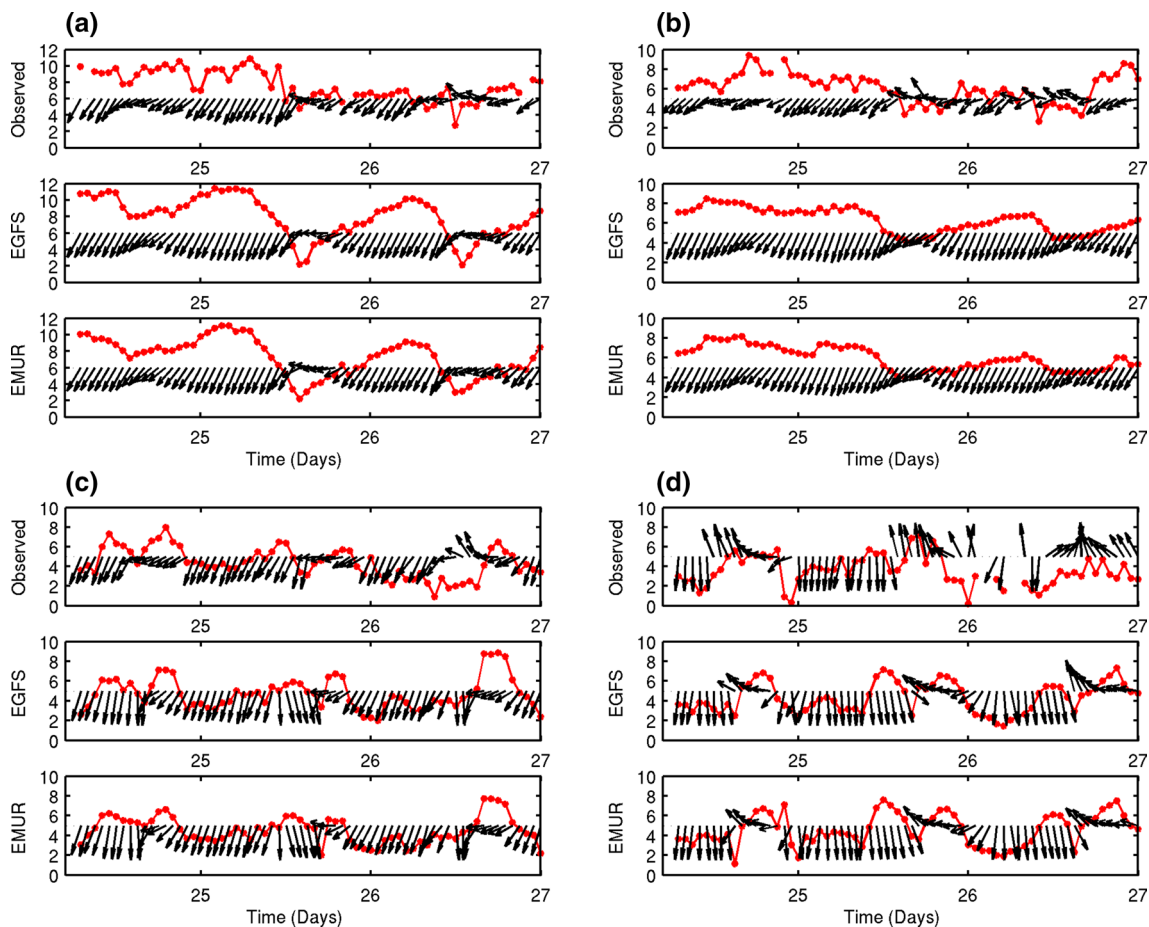
Fig. 8 Time series of the observed and simulated temperature at 2 m AGL (°C) at the **a** buoy, **b** Arraial do Cabo, **c** Macaé, **d** Marambaia sites

the mesoscale system. The numerical experiments presented similar results and adequately represent the wind during most of the evaluated period.

At the buoy site (Fig. 1), the experiments satisfactorily represented the near-surface wind throughout the evaluated period (Fig. 9a). During most of the period, the wind blows from the northeast, characterizing the SASA influence. However, during the afternoon the wind direction changes to east, evidencing the sea breeze signal.

The numerical results for Arraial do Cabo (Fig. 9b) and Macaé (Fig. 9c) sites follow the same observed temporal variation pattern. Although, the representation of the wind during the afternoon is not as sensitive to the diurnal cycle of the land–sea thermal gradient. In this period, the mesoscale system intensifies due to the enhancement of the land–sea thermal gradient and prevails the sea breeze winds superimposed on the SASA. Furthermore, the winds become more zonal and change the direction from northeast to east and southeast. However, the model seems to underestimate the mesoscale system, even with the better representation of the SST in the EMUR.

At the Marambaia site, in the border between the Central and West Coasts (Fig. 1), the measurements reveal that the near-surface wind is modulated by the land–sea breeze along the day (Fig. 9d). Since the coastline in this region is well defined in the east–west direction, during the night the land breeze blows from north, while in the afternoon the south quadrant winds characterize the presence of the sea breeze. The experiments are sensitive to this diurnal wind variation. However, as described for Arraial do Cabo and Macaé sites, the model underestimates the component of the wind characteristic of the sea breeze, which at this site is the southern component. The difficulty of satisfactorily representing the sea breeze in the coastal region of the state of Rio de Janeiro was also mentioned in Paiva et al. (2014) and Pimentel et al. (2014a). At this site, the EGFS represented the lower SST and greater land–sea thermal gradient during the afternoon (Fig. 4) and had the earliest sea breeze onset time (Fig. 9d). However, the SST modification did not have a significant impact on the wind speed and direction after the sea breeze arrives, agreeing with Knievel et al. (2010) and Sweeney et al. (2014).

Fig. 9 Time series of the observed and simulated wind at 10 m AGL (ms^{-1}) at the **a** buoy, **b** Arraial do Cabo, **c** Macaé, **d** Marambaia sites

5 Summary and conclusions

In the numerical experiments, the SST field in the coast of the state of Rio de Janeiro was represented significantly different by the MUR SST and GFS SST products. SST differences of up to 10 °C on the West Coast and 4 °C on the Central and East Coasts were verified between the experiments. The upwelling was better represented by the MUR SST. However, it is noteworthy that these satellite-derived SST products are still far from reality.

The different SST products used as initial and boundary conditions significantly impacted the T2m field, mainly over the ocean. In the region of Arraial do Cabo, influenced by the upwelling, the improvements obtained in the EMUR stand out. The observations at the buoy showed that there was no diurnal variation of T2m over the ocean at the frequency of the diurnal cycle of solar radiation. However, intriguingly, the numerical experiments which do not represent diurnal SST variation produced a well-established diurnal cycle of T2m. This result indicates that the model may be overestimating another process (e.g., horizontal advection of heat).

Between 0 and 100 m above sea level, over the offshore region, the wind was represented weaker over low SST, and stronger over high SST, which agrees with the pattern described in the literature (e.g., Wai and Stage 1989; O'neill et al. 2010; Shimada et al. 2015). Regarding wind direction, significant differences between the experiments (above 90°) occurred exclusively on the West Coast, where the greatest SST differences were verified.

The SST impact on the air temperature profile was significant up to 300 m above sea level, while the influence on the wind intensity profile was significant up to 900 m above sea level.

In all evaluated sites, a characteristic of the numerical results in comparison to the observations is highlighted. The thermal forcing is underestimated in relation to the synoptic forcing (SASA), even when there was land–sea thermal gradient intensification. When the mesoscale system (land breeze) induces wind in the same direction of the synoptic system, the model properly reproduces the wind direction near the surface. However, when the mesoscale system (sea breeze) induces wind in the opposite direction of the synoptic system, the model underestimates the thermal forcing,

culminating in larger differences between the modeled and observed wind, even with significant SST differences between experiments.

References

Ahrens DC (2009) Meteorology today: an introduction to weather, climate, and the environment, 9th edn. Brooks/Cole, Grove

Aragão LFS, Di Sabatino S, Pimentel LCG, Duda FP (2017) Analysis of the internal boundary layer formation on tropical coastal regions using SODAR data in Rio de Janeiro (Brazil). Int J Environ Pollut 62:136–154

Bravo L, Ramos M, Astudillo O, Dewitte B, Goubanov K (2016) Seasonal variability of the Ekman transport and pumping in the upwelling system off central-northern Chile (~ 30°S) based on a high-resolution atmospheric regional model. Ocean Sci 12:1049–1065

Brito TT, Oliveira-Júnior JF, Lyra GB, Gois G, Zeri M (2016) Multivariate analysis applied to monthly rainfall over Rio de Janeiro state, Brazil. Meteorol Atmos Phys. https://doi.org/10.1007/s00703-016-0481-x

Calado L, da Silveira ICA, Gangopadhyay A, de Castro BM (2010) Eddy-induced upwelling off Cape São Tomé (22°S, Brazil). Cont Shelf Res 30:1181–1188

Castelão RM (2012) Sea surface temperature and wind stress curl variability near a cape. J Phys Oceanogr 42:2073–2087

Castelão RM, Barth JA (2006) Upwelling around Cabo Frio, Brazil: the importance of wind stress curl. Geophys Res Lett 33:L03602

Castro BM, Miranda LB (1998) Physical oceanography of the western Atlantic continental shelf located between 4°N and 34°S coastal segment (4, W). In: Robinson AR, Brink KH (eds) The sea, vol 11. Wiley, New York, pp 209–251

Cataldi M, Assad LPF, Torres Junior AR, Alves JLD (2010) Estudo da influência das anomalias da TSM do Atlântico Sul extratropical na região da Confluência Brasil-Malvinas no regime hidrometeorológico de verão do Sul e Sudeste do Brasil. Rev Bras Meteorol 25:513–524

Cerda C, Castro BM (2014) Hydrographic climatology of South Brazil Bight shelf waters between Sao Sebastiao (24°S) and Cabo Sao Tome (22°S). Cont Shelf Res 89:5–14

Charnock H (1955) Wind stress on a water surface. Q J R Meteorol Soc 81:639–640

Chen T, Cobb KM, Roff G, Zhao J, Yang H, Hu M, Zhao K (2018) Coral-derived western Pacific tropical sea surface temperatures during the last millennium. Geophys Res Lett. https://doi.org/10.1002/2018GL077619

da Silva FNR, Alves JLD, Cataldi M (2018) Climate downscaling over South America for 1971–2000: application in SMAP rainfall-runoff model for Grande River Basin. Clim Dyn. https://doi.org/10.1007/s00382-018-4166-7

Dash P, Ignatov A, Martin M, Donlon C, Brasnett B, Reynolds RW, Banzon V, Beggs H, Cayula JF, Chao Y et al (2012) Group for high resolution sea surface temperature (GHRSST) analysis fields inter-comparisons. Part 2: Near real time web-based Level 4 SST Quality Monitor (L4-SQUAM). Deep-Sea Res II Top Stud Oceanogr 77–80:31–43

Dereczynski CP, Menezes WF (2015) Meteorologia da Bacia de Campos. In: Martins RP, Grossmann-Matheson GS (eds) Caracterização ambiental regional da Bacia de Campos, Atlântico Sudoeste, vol 2. Elsevier, Rio de Janeiro, pp 1–54

Dourado M, Oliveira AP (2000) Observational description of the atmospheric and oceanic boundary layers over the Atlantic Ocean. Rev Bras Oceanogr. https://doi.org/10.1590/S1679-87592001000100005

Dudhia J (1989) Numerical study of convection observed during the winter monsoon experiment using a mesoscale two-dimensional model. J Atmos Sci 46:3077–3107

Dufois F, Penven P, Whittle C, Veitch J (2012) On the warm nearshore bias in pathfinder monthly SST products over eastern boundary upwelling systems. Ocean Model 47:113–118

Emilson I (1961) The shelf and coastal waters off Southern Brazil. Bol Inst Oceanogr 11:101–112

Fragoso MR, de Carvalho GV, Soares FLM et al (2016) A 4D-variational ocean data assimilation application for Santos Basin, Brazil. Ocean Dyn 66:419–434

Franchito SH, Rao VB, Stech JL, Lorenzzetti JA (1998) The effect of coastal upwelling on the sea-breeze circulation at Cabo Frio, Brazil: a numerical experiment. Ann Geophys 16:866–881

Franchito SH, Oda TO, Rao VB, Kayano MT (2008) Interaction between coastal upwelling and local winds at Cabo Frio, Brazil: an observational study. J Appl Meteorol Climatol 47:1590–1598

Fu X, Lee J-Y, Hsu P-C, Taniguchi H, Wang B, Wang W, Weaver S (2013) Multi-model MJO forecasting during DYNAMO/CINDY period. Clim Dyn 41:1067–1081

Giannaros TM, Kotroni V, Lagouvardos K, Dellis D, Tsanakas P, Mavrellis G, Symeonidis P, Vakkas T (2017) Ultrahigh resolution wind forecasting for the sailing events at the Rio de Janeiro 2016 summer olympic games. Meteorol Appl. https://doi.org/10.1002/met.1672

Grenier H, Christopher SB (2001) A moist PBL parameterization for large-scale models and its application to subtropical cloud-topped marine boundary layers. Mon Weather Rev 129:357–377

Hashizume H, Xie S-P, Fujiwara M, Shiotani M, Watanabe T, Tanimoto Y, Liu WT, Takeuchi K (2002) Direct observations of atmospheric boundary layer response to SST variations associated with tropical instability waves over the eastern equatorial Pacific. J Clim 15:3379–3393

Hayes SP, Mcphaden MJ, Wallace JM (1989) The influence of sea surface temperature on surface wind in the eastern equatorial Pacific: weekly to monthly variability. J Clim 2:1500–1506

Hong S-Y, Dudhia J, Chen S-H (2004) A revised approach to ice microphysical processes for the bulk parameterization of clouds and precipitation. Mon Weather Rev 132:103–120

Ikeda Y (1974) Observations on the stages of upwelling in the region of Cabo Frio (Brazil) as conducted by continuous surface temperature and salinity measurements. Bol Inst Oceanogr 23:33–46

Janjic ZI (1994) The step-mountain eta coordinate model: further developments of the convection, viscous sublayer and turbulence closure schemes. Mon Weather Rev 122:927–945

Jeong JH, Song SK, Lee HW, Kim Y-K (2012) Effects of high-resolution land cover and topography on local circulations in two different coastal regions of Korea: a numerical modeling study. Meteorol Atmos Phys 118:1–20

Jiménez PA, Dudhia J (2013) On the ability of the WRF model to reproduce the surface wind direction over complex terrain. J Appl Meteorol Climatol 52:1610–1617

Jiménez PA, Dudhia J, González-Rouco JF, Navarro J, Montávez JP, García-Bustamante E (2012) A revised scheme for the WRF surface layer formulation. Mon Weather Rev 140:898–918

Jiménez PA, de Arellano JVG, Dudhia J, Bosveld FC (2016) Role of synoptic- and meso-scales on the evolution of the boundary-layer wind profile over a coastal region: the near-coast diurnal acceleration. Meteorol Atmos Phys 128:39–56

Jury M, Walker N (1988) Marine boundary layer modification across the edge of the Agulhas current. J Geophys Res 93:647–654

Knievel JC, Rife DL, Grim JA, Hahmann AN, Hacker JP, Ge M, Fisher HH (2010) A simple technique for creating regional composites of sea surface temperatures from MODIS for use in operational mesoscale NWP. J Appl Meteorol Climatol 49:2267–2284

Kucharski F, Kang I, Straus D, King MP (2010) Teleconnections in the atmosphere and oceans. Bull Am Meteorol Soc 91:381–383

LaCasse KM, Splitt ME, Lazarus SM, Lapenta WM (2008) The impact of high-resolution sea surface temperatures on the simulated nocturnal Florida marine boundary layer. Mon Weather Rev 136:1349–1372

Lazarus SM, Calvert CG, Splitt ME, Santos P, Sharp DW, Blottman PF, Spratt SM (2007) Real-time, high-resolution, space–time analysis of sea surface temperatures from multiple platforms. Mon Weather Rev 135:3158–3173

Ma Z, Fei J, Huang X, Cheng X (2014) Impacts of the lowest model level on tropical cyclone intensity and structure. Adv Atmos Sci 31:421–434

Macedo CR, Lorenzzetti JA (2015) Numerical simulations of SAR microwave imaging of the Brazil current surface front. Braz J Oceanogr. https://doi.org/10.1590/S1679-87592015082306304

Martin M, Dash P, Ignatov A, Banzon V, Beggs H, Brasnett B, Cayula J-F, Cummings J, Donlon C, Gentemann C, Grumbine R, Ishizaki S, Maturi E, Reynolds RW, Roberts-Jones J (2012) Group for high resolution sea surface temperature (GHRSST) analysis fields inter-comparisons. Part 1: A GHRSST multi-product ensemble (GMPE). Deep-Sea Res II 77–80:21–30

Mazzini PLF, Barth JA (2013) A comparison of mechanisms generating vertical transport in the Brazilian coastal upwelling regions. J Geophys Res Oceans 118:1–17

Messager C, Faure V (2012) Validation of remote sensing and weather model forecasts in the Agulhas ocean area to 57°S by ship observations. S Afr J Sci. https://doi.org/10.4102/sajs.v108i3/4.735

Mill GN, da Costa VS, Lima ND, Gabioux M, Guerra LAA, Paiva AM (2015) Northward migration of Cape São Tomé rings, Brazil. Cont Shelf Res 106:27–37

Mlawer EJ, Taubman SJ, Brown PD, Iacono MJ, Clough SA (1997) Radiative transfer for inhomogeneous atmosphere: RRTM, a validated correlated-k model for the longwave. J Geophys Res 102:16663–16682

Moisseeva N, Steyn DG (2014) Dynamical analysis of sea-breeze hodograph rotation in Sardinia. Atmos Chem Phys 14:13471–13481

Niu G-Y, Yang Z-L, Mitchell KE, Chen F, Ek MB, Barlage M, Kumar A, Manning K, Niyogi D, Rosero E, Tewari M, Xia Y (2011) The community Noah land surface model with multiparameterization options (Noah—MP): 1. Model description and evaluation with local-scale measurements. J Geophys Res 116:D12109

O'Neill LW, Esbensen SK, Thum N, Samelson RM, Chelton DB (2010) Dynamical analysis of the boundary layer and surface wind responses to mesoscale SST perturbations. J Clim 23:559–581

Oliveira-Júnior JF, Pimentel LCG, Landau L (2010) Critérios de estabilidade atmosférica para a região da Central Nuclear Almirante Álvaro Alberto, Angra dos Reis—RJ. Rev Bras Meteorol 25:270–285

Paiva LM, Bodstein GCR, Pimentel LCG (2014) Influence of high-resolution surface databases on the modeling of local atmospheric circulation systems. Geosci Model Dev 7:1641–1659

Palóczy A, da Silveira ICA, Castro BM, Calado L (2014) Coastal upwelling off Cape São Tomé (22°S, Brazil): the supporting role of deep ocean processes. Cont Shelf Res 89:38–50

Peres LF, França GB, Paes RC, Sousa RC, Oliveira AN (2017) Analyses of the positive bias of remotely sensed SST retrievals in the coastal waters of Rio de Janeiro. IEEE Trans Geosci Remote Sens 55:6344–6353

Phan TT, Manomaiphiboon K (2012) Observed and simulated sea breeze characteristics over Rayong coastal area, Thailand. Meteorol Atmos Phys 116:95–111

Pimentel LCG, Barbosa CE, Marton E, Cataldi M, Nogueira E (2014a) Influência dos parâmetros de configuração do modelo CALMET sobre a simulação da circulação atmosférica na região metropolitana do Rio de Janeiro. Rev Bras Meteorol 29:579–596

Pimentel LCG, Marton E, Soares da Silva M, Jourdan P (2014b) Caracterização do regime de vento em superfície na Região Metropolitana do Rio de Janeiro. Rev Eng Sanit Ambient 19:121–132

Reynolds RW, Rayner NA, Smith TM, Stokes DC, Wang W (2002) An improved in situ and satellite SST analysis for climate. J Clim 15:1609–1625

Ribeiro FND, Soares J, Oliveira AP (2011) The co-influence of the sea breeze and the coastal upwelling at Cabo Frio: a numerical investigation using coupled models. Braz J Oceanogr 59:131–144

Ribeiro FND, Soares J, Oliveira AP (2016) Sea-breeze and topographic influences on the planetary boundary layer in the coastal upwelling area of Cabo Frio (Brazil). Bound Layer Meteorol 158:139–150

Rodrigues RR, Lorenzzetti JA (2001) A numerical study of the effects of bottom topography and coastline geometry on the Southeast Brazilian coastal upwelling. Cont Shelf Res 21:371–394

Santos TP, Franco DR, Barbosa CF, Belem AL, Dokken T, Albuquerque ALS (2013) Millennial- to centennial-scale changes in sea surface temperature in the tropical South Atlantic throughout the Holocene. Palaeogeogr Palaeoclimatol Palaeoecol 392:1–8

Scheel-Ybert R (2000) Vegetation stability in the Southeastern Brazilian coastal area from 5500 to 1400 14C yr BP deduced from charcoal analysis. Rev Palaeobot Palynol 110:111–138

Seroka G, Miles T, Dunk R, Kohut J, Glenn S, Fredj E (2015) Sea breeze, coastal upwelling modeling to support offshore wind energy planning and operations. MTS/IEEE OCEANS (Washington, USA). https://doi.org/10.23919/oceans.2015.7404456

Shimada S, Ohsawa T, Kogaki T, Steinfeld G, Heinemann D (2015) Effects of sea surface temperature accuracy on offshore wind resource assessment using a mesoscale model. Wind Energy 18:1839–1854

Shin HH, Hong SY, Dudhia J (2012) Impacts of the lowest model level height on the performance of planetary boundary layer parameterizations. Mon Weather Rev 140:664–682

Silva FP, Rotunno Filho OC, Sampaio RJ, Dragaud ICDV, Magalhães AAA, Justi da Silva MGA, Pires GD (2017) Evaluation of atmospheric thermodynamics and dynamics during heavy-rainfall and no-rainfall events in the metropolitan area of Rio de Janeiro. Brazil. Meteorol Atmos Phys. https://doi.org/10.1007/s00703-017-0570-5

Skamarock WC, Klemp JB, Dudhia J, Gill DO, Barker DM, Duda M, Huang XY, Wang W, Powers JG (2008) A description of the advanced research WRF version 3. In: Technical report, TN-475+STR, NCAR

Song Q, Cornillon P, Hara T (2006) Surface wind response to oceanic fronts. J Geophys Res 111:C12006

Song Q, Chelton DB, Esbensen SK, Thum N, O'Neill LW (2009) Coupling between sea surface temperature and low-level winds in mesoscale numerical models. J Clim 22:146–164

Sproson D, Sahlée E (2014) Modelling the impact of Baltic Sea upwelling on the atmospheric boundary layer. Tellus A 66:1–15

Stech JL, Lorenzzetti JA (1992) The response of the South Brazil Bight to the passage of wintertime cold fronts. J Geophys Res 97:9507–9520

Stull RB (1988) Introduction to boundary layer meteorology. Kluwer Academic Press, Dordrecht, p 666

Sweeney JK, Chagnon JM, Gray SL (2014) A case study of sea breeze blocking regulated by sea surface temperature along the English south coast. Atmos Chem Phys 14:4409–4418

Sweet W, Fett R, Kerling J, La Violette P (1981) Air–sea interaction effects in the lower troposphere across the north wall of the Gulf Stream. Mon Weather Rev 109:1042–1052

Tseng YH, Chien SH, Jin J, Miller NL (2012) Modeling air–land–sea interactions using the integrated regional model system in Monterey Bay, California. Mon Weather Rev 140:1285–1306

Valentin JL, Andre DL, Jacob SA (1987) Hydrobiology in the Cabo Frio (Brazil) upwelling: two-dimensional structure and variability during a wind cycle. Cont Shelf Res 7:77–88

Vazquez-Cuervo J, Dewitte B, Chin TM, Armstrong EM, Purca S, Alburqueque E (2013) An analysis of SST gradients off the Peruvian Coast: the impact of going to higher resolution. Remote Sens Environ 131:76–84

Wai M, Stage SA (1989) Dynamical analysis of marine atmospheric boundary layer structure near the Gulf Stream oceanic front. Q J R Meteorol Soc 115:29–44

Wallace JM, Mitchell TP, Deser CJ (1989) The influence of sea surface temperature on surface wind in the eastern equatorial Pacific: weekly to monthly variability. J Clim 2:1492–1499

Wiafe G, Nyadjro ES (2015) Satellite observations of upwelling in the Gulf of Guinea. IEEE Geosci Remote Sens Lett 12:1066–1070

World Meteorological Organization (2008) Guide to meteorological instruments and methods of observation, 7th edn. Secretariat of the World Meteorological Organization, Geneva

Yang Z-L, Niu G-Y, Mitchell KE, Chen F, Ek MB, Barlage M, Longuevergne L, Manning K, Niyogi D, Tewari M, Xia Y (2011) The community Noah land surface model with multiparameterization options (Noah-MP): 2. Evaluation over global river basins. J Geophys Res 116:D12110